

DNS of Laminar to Turbulent Transition on NACA 0012 Airfoil with Sand Grain Roughness

A.F.P. Ribeiro,* E. Fares,* and M. Choudhari**

Corresponding author: andre@exa.com

* Exa GmbH, Stuttgart, Germany

** NASA Langley Research Center, Hampton, VA, USA

Abstract: The Lattice-Boltzmann-based solver PowerFLOW is used to perform direct numerical simulations of the transitional flow over an airfoil at Reynolds number equal to 0.657 million. The leading edge of the airfoil is covered with sand particles, represented by polyhedra, to mimic the grit used in experiments. The sensitivity of the laminar to turbulent transition to the size of these particles, grid resolution, spanwise length is evaluated and rectangular trips are also tested.

Keywords: Lattice Boltzmann Method, direct numerical simulation, grit, tripping devices.

1 Introduction

In the context of the Benchmark Problems for Airframe Noise Computations (BANC [1]) workshop, simulations of trailing edge (TE) noise of airfoils have been conducted with several methodologies [2]. While semi-analytical methods can be used to predict such noise [3-6], high-fidelity Computational Fluid Dynamics (CFD) continues to grow in usage, with the distinct advantage of being general purpose, allowing for different noise generation as well as noise reduction mechanisms, and simultaneous prediction of aerodynamic properties from a single simulation [7, 8]. The CFD code PowerFLOW, based on the Lattice-Boltzmann method (LBM), has been used to calculate the trailing edge noise both in an industrial setting by using turbulence modeling [9] and in an academic context, through direct numerical simulations [10]. The current work expands on the latter, focusing on the aerodynamics.

Both the level and the spectral distribution of the acoustic field radiated from the airfoil are functions of the boundary layer thickness just upstream of the trailing edge, which in turn depends on the location of laminar-turbulent transition in the boundary layer flow. To minimize the sensitivity of the transition process to the details of the freestream disturbance environment, boundary layer tripping is often used to ostensibly fix the transition location and to ensure an easier to reproduce, fully turbulent boundary layer flow ahead of the trailing edge location. However, despite many decades of employing boundary layer trips in wind tunnel experiments, trip design continues to be an empirical art rather than science, which can lead to considerable variability in transition location and hence in the boundary layer parameters near the trailing edge. Due to the uncertainty in determining optimal trip parameters for a given application, conservative trip designs, i.e., larger than necessary trip heights are often used to ensure transition within the short distance behind the trip. The over tripping of the boundary layer flow can also add to the uncertainty in boundary layer thickness immediately behind the trip, as well as introducing a spanwise distortion of the mean flow in the wake. For deterministic trips such as zigzag tapes, over tripping can introduce strong periodic structures in the boundary layer flow that can persist for long distances into the trip wake, even after the flow has become fully turbulent. Trip induced flow

distortion can potentially influence the trailing edge noise, and there is experimental evidence that trips may result in an additional source of noise associated with the interaction of unsteady vorticity structures in the transitional boundary layer with the surface deformation associated with the trips.

These extraneous mechanisms related to the transition process add further to the variability among the different measurements of the same airfoil geometry at similar flow conditions. In particular, phased microphone array measurements [11] have shown that scrubbing noise due to grit near the leading edge (LE) can overpower the trailing edge noise at higher frequencies. The grit-induced noise had been filtered out in the earlier measurements [12, 13], since they used the Coherent Output Power (COP) method, which is based on a cross-spectral analysis of pairs of output signals from microphones placed around the model airfoil. Acoustic measurements of the NACA 0012 airfoil [14] also indicated peculiar discrepancies with the measurements by Brooks, Pope, and Marcolini [15]. Again, differences in tripping and acoustic measurement techniques were suggested as possible reasons behind these discrepancies.

Modeling the transition process within the CFD computation is also important in purely aerodynamic simulations. According to the CFD 2030 Vision of the NASA Revolutionary Computational Aerosciences (RCA) subproject [16], the most critical area in computational fluid dynamics (CFD) simulation capability that will remain a pacing item in the analysis and design of aerospace systems by 2030 is the ability to adequately predict viscous turbulent flows with boundary layer transition and flow separation. Specifically, physics-based predictive capability for boundary layer transition is one of the important set of capabilities required for satisfying the requirements outlined in 2030 Vision CFD. Presently, many CFD design processes include an estimation of boundary layer transition based on models ranging in fidelity from purely empirical to semi-empirical ones based on the amplification of hydrodynamic instability waves. Because of the complexity of the transition process and its sensitivity to disturbance environment, no generalized transition prediction capability is in widespread use in Navier-Stokes CFD and the commonly adopted approach is running such codes in a fully turbulent mode without any transition modeling. When transition is simulated in lieu of being modeled, the number of cells within the laminar and transitional regions is 10 to 100 times larger than that in the turbulent region. Therefore, the cost of simulating the transitional region has been identified as a major bottleneck to high fidelity computations in aerospace applications.

In the context of subscale wind tunnel experiments, boundary layer tripping is most commonly accomplished via mechanical trips in the form of 2D trip wires [17], 3D but deterministic zigzag tapes [18], or distributed roughness in the form of grit [15] or other roughness distributions [19-21]. On the other hand, nearly all of the previous numerical simulations involving intentional boundary layer tripping have used artificial, numerical trip devices such as localized suction and blowing [22, 23]. An exception to this practice appears to be the LES by Winkler et al. [24], which used an array of triangular-planform trips mounted within the front portion of the airfoil to trip the boundary layer. In comparison with the triangular trips, the nominally stochastic pattern of surface mounted grit or sand grain roughness is likely to reduce the flow distortion in the fully turbulent region and is often used during subscale tests in lieu of a deterministic trip. Distributed roughness of this type can also occur naturally in aerodynamic applications, either as a result of degradation of the surface over time or due to manufacturing imperfections or, in the case of hypersonic vehicles, arises as a byproduct of surface ablation due to aerodynamic heating of the vehicle surface. Current modeling of distributed-roughness effects is primarily empirical and no single correlation appears to capture all of the relevant physics for both engineered and service-related roughness. Therefore, simulations are needed to enhance the understanding of transition mechanisms so that physics-based predictive models can be developed and validated in detail. Because of the geometric complexity of sand grain roughness, modeling the flow over an airfoil with grit has not been investigated thus far.

The current work is organized as follows: section 2 provides a brief description of the numerical method used for the simulations. A description of the test case, including the different grits and trips used is given in section 3. Simulation results are shown in section 4. Section 5 draws conclusions based on the results and indicates future work that will be conducted in this context.

2 Numerical Method

The Lattice-Boltzmann equation has the following form [25, 26]:

$$f_i(\vec{x} + \vec{c}_i \Delta t, t + \Delta t) - f_i(\vec{x}, t) = C_i(\vec{x}, t) \quad (1)$$

where f_i is the particle density function, which represents the probability for particles to travel with speed c from the position x at time t in the direction i . The travel speed is chosen so that particles travel one cell in one time step, effectively making the CFL number [27] for f_i equal to one. The collision term C_i is modeled with the well-known BGK approximation [28] as follows:

$$C_i(\vec{x}, t) = -\frac{1}{\tau} [f_i(\vec{x}, t) - f_i^{eq}(\vec{x}, t)] \quad (2)$$

where τ is the relaxation time, which relates to the fluid viscosity ν with the relation $\nu = a^2(\tau - \Delta t/2)$, where a is the speed of sound and Δt is the time step. The term f_i^{eq} is the equilibrium distribution, which is approximated by a third order expansion [29]:

$$f_i^{eq}(\vec{x}, t) = \rho \omega_i \left(1 + \frac{\vec{c}_i \cdot \vec{u}}{T_0} + \frac{(\vec{c}_i \cdot \vec{u})^2}{2T_0^2} - \frac{\vec{u}^2}{2T_0} + \frac{(\vec{c}_i \cdot \vec{u})^3}{6T_0^3} - \frac{(\vec{c}_i \cdot \vec{u})\vec{u}^2}{2T_0^2} \right) \quad (3)$$

where ρ is the fluid density, ω_i is the weight function, which depends on the direction being calculated, u the fluid velocity, and T_0 the temperature, which is set to 1/3, in lattice units, for isothermal cases [30]. To recover the fluid quantities from f_i , the Chapman-Enskog expansion is employed [31], which yields:

$$\rho(\vec{x}, t) = \sum_i f_i(\vec{x}, t) \quad (4)$$

$$\rho \vec{u}(\vec{x}, t) = \sum_i \vec{c}_i f_i(\vec{x}, t) \quad (5)$$

PowerFLOW 5.4b solves the D3Q19 (3 dimensions, 19 velocity states) formulation of the Lattice-Boltzmann equation for. This has been demonstrated to correspond to solving the Navier-Stokes equations [32-34] at the continuum limit. The interaction of a laminar boundary layer with a grit strip and the consequent transition to turbulence requires a level of spatial and temporal resolution that is compatible with DNS. Hence the turbulence modeling capability of PowerFLOW [35] is not used for the present simulations.

The LBM is solved on a grid composed of cubic volumetric elements (voxels). A variable resolution by a factor of two is allowed between adjacent regions. Consistently, the time step is varied by a factor two between two adjacent resolution regions. Solid surfaces are automatically facetized within each voxel intersecting the wall geometry. This facetization creates planar surface elements, named surfels [36]. Time advancement is performed with an explicit scheme, which allows for efficient, highly-scalable simulations.

The numerical methods described have been extensively validated for a wide variety of applications. Relevant to this study are other direct numerical simulations [37], including trailing edge noise at lower Reynolds numbers with transition being triggered by a laminar separation bubble [38]. In addition, the current methodology has also been used for several applications at higher Reynolds numbers with turbulence modeling. This includes aerodynamic simulations of airfoils [39] and full wings [40], and aeroacoustics of full aircraft [41].

3 Test Case Description

This paper follows the previous work [3] that was focused on the computation of trailing edge noise. The flow configuration of interest corresponds to an NACA 0012 airfoil at a Reynolds number of 0.657 million based on the aerodynamic chord and a Mach number of 0.1155. The initial simulations used a

spanwise domain of 1.875% of the chord, with periodic boundary conditions. In this work, the spanwise domain is initially reduced by 3 times then extended up to 7 times (or 2.33 times the original), to allow the large turbulent structures to develop properly. The finest elements of the volume mesh are located on the leading and trailing edges of the airfoil. The finest element size is 0.002% of the chord, which corresponds to 30 voxels per sphere diameter, 15 voxels across the trailing edge thickness, 768 voxels per span (for the 1.875% span), and an average y^+ of 0.5 over the airfoil. The grid was constructed so that the boundary layer fits inside the two finest regions, followed by quick coarsening after that. There are approximately 1800 voxels across the boundary layer thickness near the airfoil trailing edge. The case with the smallest span has a total of 3.93 billion voxels and the largest span configuration has 12.4 billion voxels.

The experiments used a commercial grit #60 over the first 20 percent of the airfoil chord on both top and bottom surface. The mean particle diameter is 0.29 mm and the packing density over the airfoil surface is specified as 3.8 particles/mm². This grit is approximated in the simulations by a distribution of icosahedra with a mean diameter equal to the mean particle size and the same packing density as in the experiment. Also, due to a lack of information concerning the distribution of particle size in the experiment, the particle diameter is assumed to have a Gaussian distribution with a standard deviation of 5% of the sphere diameter. Previously [10], the particles were modeled as half sunk into the adhesive layer, which effectively halved their height and is likely the reason for the late transition observed during the simulations. The current simulations are based on the best available estimates of the adhesive thickness, which is small in comparison with the grit size. Consequently, the particles stick out of the airfoil almost entirely, being sunk by just 0.03 mm, which is the expected adhesive thickness, although the adhesive itself is not modeled, i.e., the underlying surface is identical to the NACA 0012 airfoil. The particles are first scattered over the surface homogeneously, but then shifted in a random direction parallel to the surface by a distance dictated by a Gaussian distribution with a standard deviation of 1 particle diameter. Approximately 4 particles are present over the spanwise width of the computational domain for the smallest span. Particles that are cut by the periodic boundary conditions are split in two and the part that would have been outside of the domain is translated to the other side of the span. Each individual particle is oriented (i.e., rotated around its center) randomly. A close-up of the grit on the airfoil with the largest span is shown in Fig. 1.

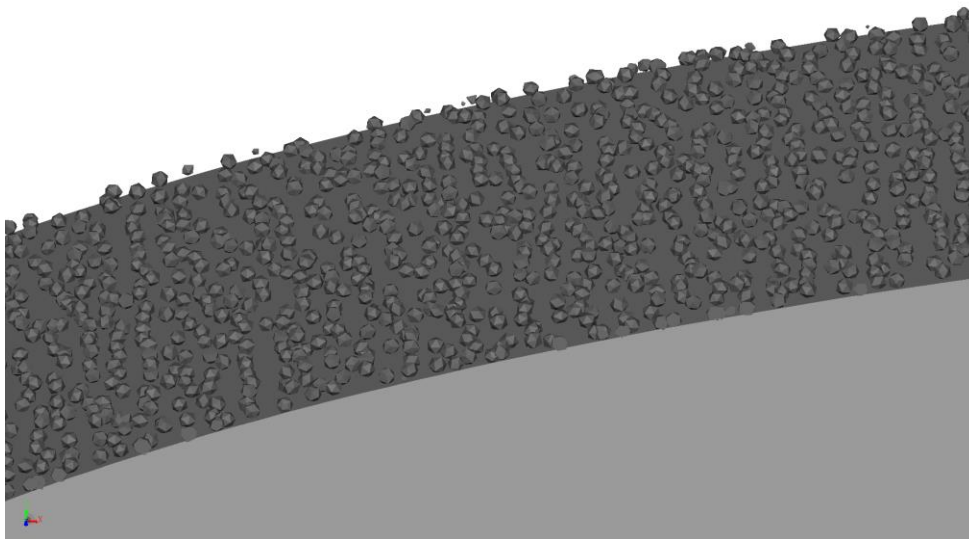


Figure 1: Grit distribution near 7% chord for the case with a spanwise domain width of 4.375% chord.

The simulation requires about 1.5 flow passes for the initial transient and was run for at least another flow pass for statistical sampling. Since the case with the smallest span requires about 160,000 CPU

hours per flow pass, this makes running a large number of cases rather expensive. Hence, two cost-cutting measures are tested. The first is placing a chordwise-spanwise symmetry plane through the center of the airfoil. This makes the simulation unusable from a trailing edge noise perspective, but may still allow for transition computations. This hypothesis is tested in the next section. The second measure is to coarsen the grid starting at 30% of the chord. This means the boundary layer is not properly resolved over the entire airfoil, but may still allow for the region where transition occurs to be accurately captured, as long as the flow becomes fully turbulent within 30% of the chord. This hypothesis is also tested in the next section. Using both of these cost-cutting measures at the same time reduces the CPU hours required for the case by about 5 times, allowing larger spans to be computed without making the simulations unaffordable.

4 Results

The results in this section are presented as follows: section 4.1 demonstrates the viability of running the transition simulations with only the upper half of the airfoil, and also clarifies the effects of both refining the leading edge of the airfoil and coarsening the downstream part. Section 4.2 describes the computational results for various grit heights as well as the impact of using alternate trip configurations in the form of a homogeneous grit distribution, a rectangular trip configuration, and CAD dot trips, respectively. Section 4.3 presents the results for larger spans, ranging from $L_z/c = 0.625\%$ to 4.375% , corresponding to a seven-fold variation in the spanwise width of the computational domain.

In general, as in [10], the main metric for identifying the transition location in this work is the spanwise averaged standard deviation of the pressure coefficient, or the root mean square of pressure coefficient fluctuations ($C_{p,RMS}$) on the surface of the airfoil. The skin friction coefficient (C_f) is also a useful quantity to detect transition; however, it fluctuates dramatically in the presence of particles, which introduces local stagnation points, rapid flow acceleration, as well as multiple regions of local separations. In the cases studied here, the rise in $C_{p,RMS}$ consistently agreed with the rise in C_f , but was generally easier to determine. The boundary layer displacement thickness (δ^*) and boundary layer momentum thickness (θ) are also reported for select cases.

4.1 Symmetry Plane and Resolution Sensitivity

In order to achieve a large number of computations, the computational cost per run had to be reduced. The first way to reduce the cost so was to place a chordwise-spanwise symmetry plane across the center of the symmetric airfoil, effectively only running the simulation for the upper half of the airfoil. This simulation is used as the baseline for all other runs. This could be done because the focus of the current work is on the laminar to turbulent transition, and not on the trailing edge noise. Of course, upstream feedback from the unsteady interactions near the trailing edge can still influence the boundary layer transition process; therefore, comparisons are made to assess the significance of the acoustic feedback on the transition location. Additionally, the possibility of coarsening the mesh in the downwind part of the airfoil, from 30% of the chord up to the trailing edge while maintaining the same grid within the upstream portion of the airfoil was also tested. Finally, in order to verify that the resolution on the leading edge is sufficient, the volume mesh near the grit was refined by a factor of 2 in each direction. A summary of these cases is shown in Table 1. All of the cases have a span of 0.625% chord.

Table 1: Summary of cases for the mesh and symmetry sensitivity studies.

Case name	Symmetry plane	Mesh
Baseline	yes	Baseline
No Symmetry	no	Baseline
Fine LE	yes	2x refined LE
Coarse TE	yes	2x coarse after 30% chord

Good agreement between the flow metrics of interest for the Baseline and the No Symmetry cases will

indicate that a symmetry plane can be used for the computations from the next subsections. Good agreement between Baseline and Fine LE cases will show that the baseline resolution of the grit is sufficient for this configuration. Good agreement between the baseline and Coarse TE will mean that longer spans can be computed by using the coarser grid within the post-transitional region of the airfoil, to save on the overall computational cost. Results for all of these cases are shown in Fig. 2 in the form of $C_{p,RMS}$ distributions over the chord of the airfoil, averaged over the span. As previously mentioned, this is smoother than the C_f distribution and indicates transition in the same location for all cases presented here. As expected, the pressure fluctuation values start close to zero near the stagnation point. The No Symmetry configuration shows slightly higher values on the leading edge, likely due to nonzero lift fluctuations caused by the unsteadiness near the trailing edge, making the stagnation point move slightly in time. $C_{p,RMS}$ then rises quickly around 3% chord for all cases, indicating they are all transitioning to turbulence at the same location. The Baseline and Fine LE cases are very similar throughout the chord, with small fluctuations that are likely due to the limitations of statistical convergence. The No Symmetry is also very close to the Baseline from the LE up to 30% chord, which is the region of interest in this work. Finally, the Coarse TE case shows higher values of pressure fluctuations than all the other cases on the second half of the airfoil, likely because the coarser mesh induces larger flow structures, which are more energetic. Most significantly, however, all of these cases show very similar results from the leading edge up to 30% chord, indicating that all of the hypotheses listed at the beginning of this paragraph are valid, i.e., the mesh on the grit region does not seem to require additional refinement to predict transition, a symmetry plane does not shift the transition location, and coarsening the downwind part of the airfoil does not affect the predictions within the upwind part. With that in mind, subsection 4.2 will use a symmetry plane for all its runs and subsection 4.3 will use both a symmetry plane and a coarser mesh downstream unless stated otherwise.

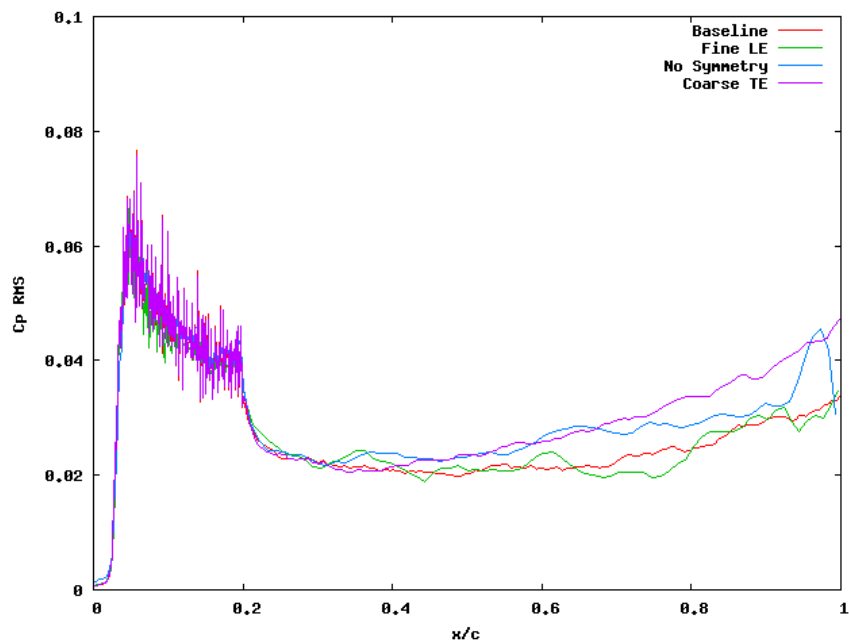


Figure 2: $C_{p,RMS}$ over the airfoil chord.

4.2 Grit Height and Trip Type Sensitivity

The purpose of this section is to investigate the minimum grit height to achieve transition within the region of the grit, while also testing alternate tripping devices that are more deterministic than the stochastic grit distribution. Because comparing these cases will require looking at flow properties throughout the entire airfoil chord, no coarsening is used. However, since TE noise is being neglected, all runs employ a symmetry plane. Table 2 summarizes the cases described in this subsection. All of the cases have a span of 0.625% chord.

Table 2: Summary of cases for sensitivity study related to grit height and trip type.

Case name	Trip height (mm)	Trip type
Baseline	0.29	Grit
Grit 85%	0.25	Grit 85% smaller than baseline
Grit 75%	0.22	Grit 75% smaller than baseline
Grit 65%	0.17	Grit 65% smaller than baseline
Homogeneous Grit	0.29	Equally spaced grit
Trip Strip	0.36	Rectangular
Trip Strip 85%	0.31	Rectangular
Dot Trip	0.31	Cylinder

All of the Grit cases have particles applied up to 20% of the chord. The number next to the Case name in Table 2 refers to the grit height relative to the Baseline case. The first set of cases after the Baseline are tested to verify the minimum grit height, an important factor when attempting not to overtrip the boundary layer flow. The Homogeneous Grit case uses a grit that is identical to the baseline case in both particle size and density, but with no randomness in position, orientation, and size of the particles. Hence, identical particles are positioned in an equispaced pattern over the first 20% of the airfoil chord. The Trip Strip and Trip Strip 85% configurations refer to rectangular trips placed at 5% of the chord. Finally, the Dot Trip is composed of a cylinder placed at 5% of the chord, which represents a spanwise periodic array of cylinders because of the periodic boundary conditions in the spanwise direction. The four grit types are shown in Fig. 3.

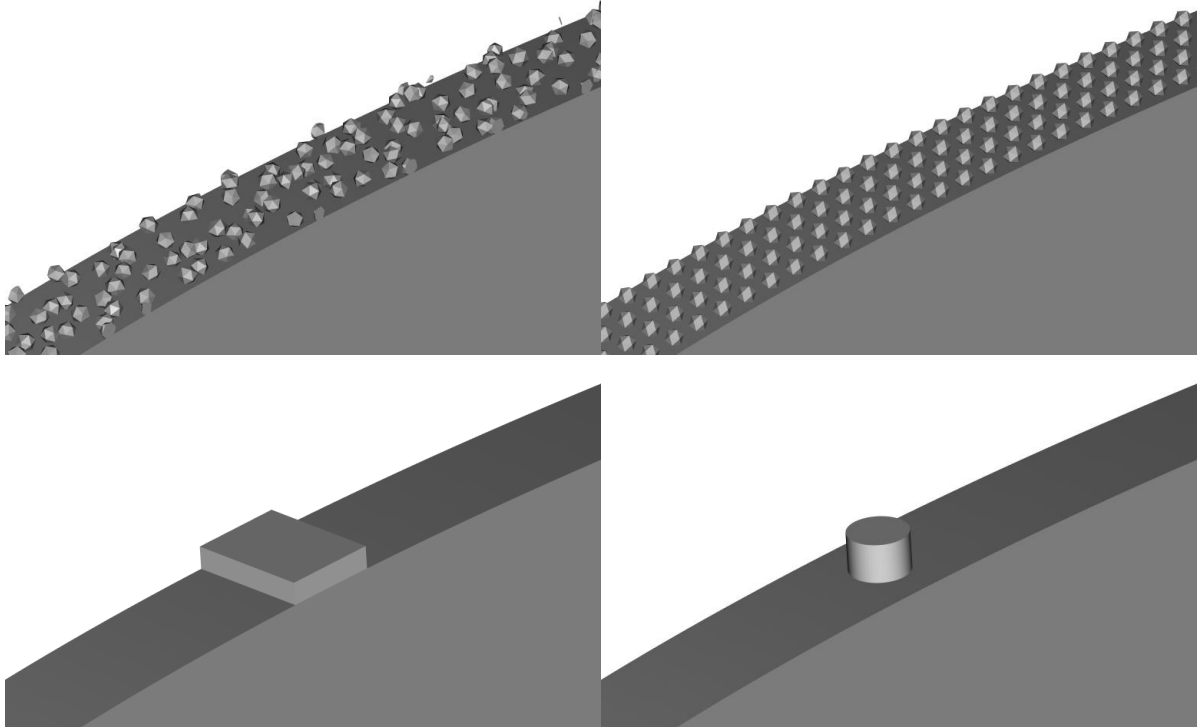


Figure 3: Different grit types used in subsection 4.2. Top left: Baseline, top right: Homogeneous Grit, bottom left: Trip Strip, bottom right: Dot Trip.

Fig. 4 shows $C_{p,RMS}$ over the chord for the cases with the randomly scattered grit with variable height. As the grit height is reduced from the baseline case up to 75% height, the transition point gradually shifts further downstream, as expected. As the height parameter is further reduced to 65% of the original height, the onset of fully turbulent flow no longer occurs within the region of the grit (i.e., within the first 20% of the chord), moving significantly aft to about 65% of the chord. The abrupt movement in

transition location indicates a threshold or “effective” roughness height of between 65% and 75% for the transition to occur within the grit region. The substantially aft transition location for the 65% height is similar to the results in [10], where the particles were half sunk into the airfoil, effectively reducing their height by a factor of 2. These findings indicate a change in the transition physics from the effective height cases (approximately 75% and above) to those with smaller roughness heights; however, further analysis is necessary to establish those differences.

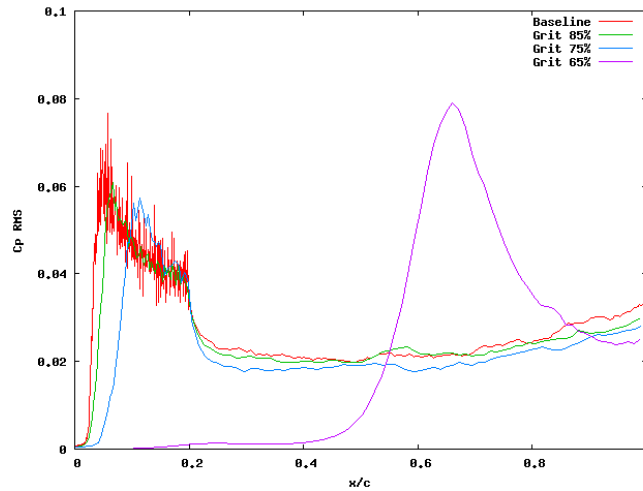


Figure 4: $C_{p,RMS}$ over the airfoil chord for different grit heights.

Fig. 5 shows the $C_{p,RMS}$ for the additional cases described in Table 2. All of those methods for tripping successfully transition the flow into turbulence before 20% chord. Homogeneous Grit shows a later onset of transition compared to the Baseline, which is investigated in Fig. 9. However, because the stochastic height distribution in the Baseline case involves variations in both the particle spacing and the shape parameters (height, orientation, etc.), it is difficult to determine the dominant cause behind the later onset of transition in the Homogeneous Grit case. Reducing the trip strip height to 85% still leads to transition, which means that the baseline Trip Strip is larger than the minimum height required to induce boundary layer transition near the leading edge. The Dot Trip and the Trip Strip seem to behave almost identically, other than a local peak in $C_{p,RMS}$ in the immediate vicinity of the trip strip.

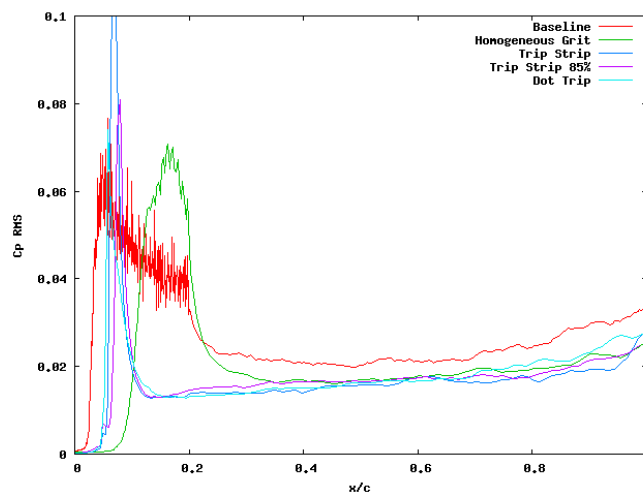


Figure 5: $C_{p,RMS}$ over the airfoil chord for different trip types.

As a measure of overtripping, the drag coefficient for the cases in this subsection is shown in Fig. 7. Results for XFOIL [42] tripped at 5% are also shown as reference. Results consistently show a reduction in drag with decreasing trip height, as expected. The Grit 65% case is clearly an outlier due to having

mostly laminar flow, while Trip Strip 85% seems to be the least intrusive, introducing the smallest amount of drag. Even though the Homogeneous Grit case had the latest onset of transition (other than Grit 65%), it still has a higher drag than the Trip Strip cases. This is due to the local drag introduced by the trip, due to local separations, stagnations, and accelerations. Results for the Homogeneous Grit and Dot Trip cases agree particularly well with XFOil.

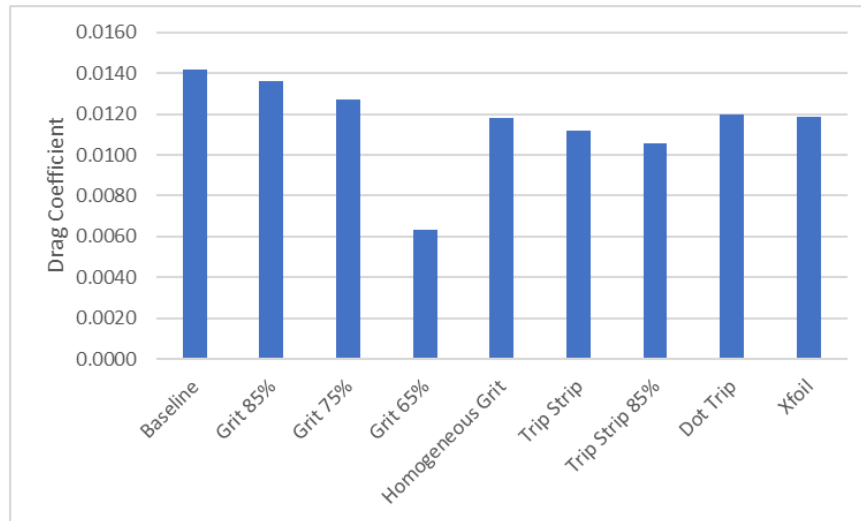


Figure 6: Mean drag coefficient for all the cases in this subsection and in XFOil.

The time-averaged values of boundary layer displacement thickness, δ^* and momentum thickness, θ , at the midspan location are reported for all cases from this subsection in Figs. 7 and 8, respectively, and are also compared to values from XFOil (tripped at 5%) and the experiments by Brooks et al. [15].

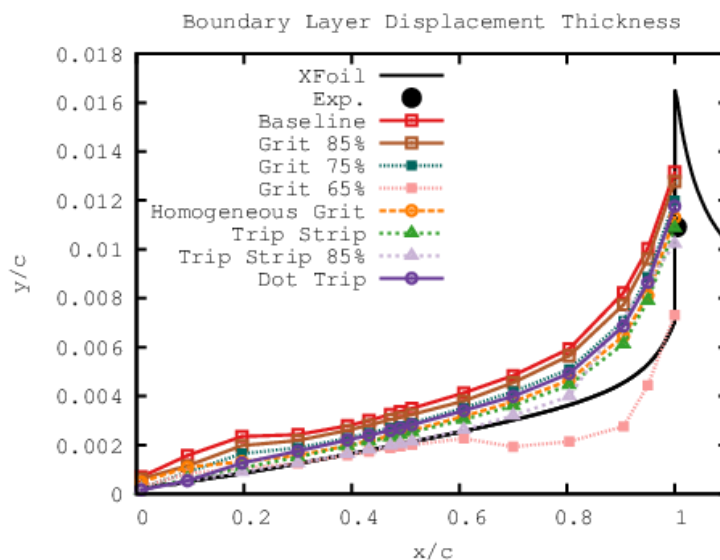


Figure 7: Boundary layer displacement thickness for all cases in this subsection compared to XFOil and experimental data.

The current set of predictions for δ^* and θ compare significantly better with experiments relative to the previous simulations in [10], which had effectively half the grit height. The comparison with experiments further suggests that the grit distribution used in the experiment was sufficient to induce transition within the region of the grit. Although not shown, we note that the boundary layer thickness at the end of the grit region, i.e., $\delta_{0.99}(x/c = 0.20)$ varies from approximately 0.59% of the chord for the Homogeneous Grit case to 0.95% of the chord for the Dot Trip case. Thus, the spanwise domain width

is at least 66% the boundary layer thickness at the beginning of the fully turbulent region.

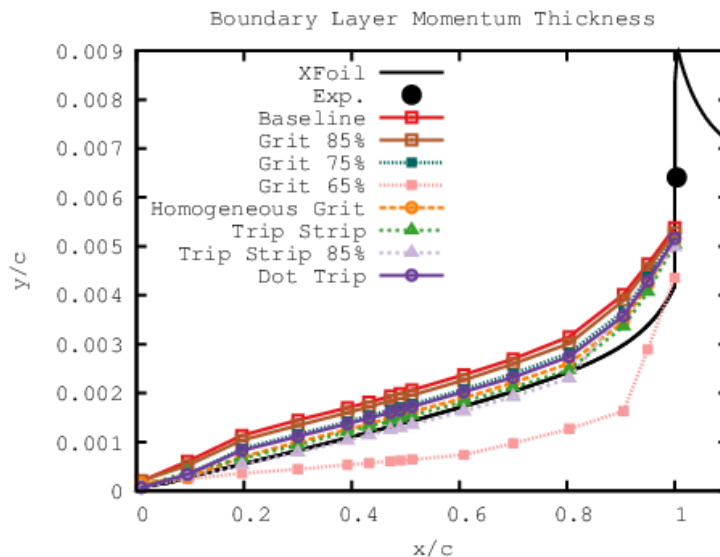


Figure 8: Momentum thickness for all cases in this subsection compared to Xfoil and experimental data.

The surface distribution of $C_{p,RMS}$ near the transition location is shown in Fig. 9. In comparison with the Baseline case, the Homogeneous Grit clearly shows significantly less spanwise variation in the transition front identified by the rapid rise in $C_{p,RMS}$. This behavior is attributed to the random nature of the grit distribution, which leads to greater spanwise variability in the flow depending on the details of this distribution. The spanwise variations across the transition front are further explored in subsection 4.3.

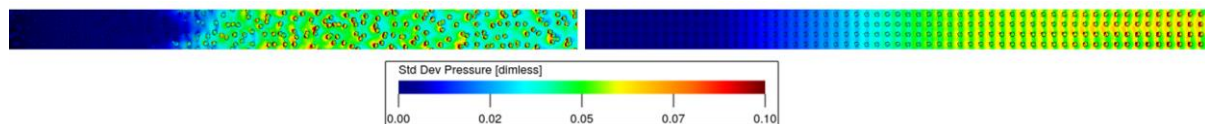


Figure 9: surface distribution of $C_{p,RMS}$ near the transition location. Baseline on the left, Homogeneous Grit on the right.

Fig. 10 shows the λ_2 [43] isosurfaces near the transition location for selected trip configurations. Even though a substantially deeper analysis of the simulation database is yet to be performed, the flow structures in this figure provide partial clues regarding the likely transition mechanism in each case. The Homogeneous Grit case displays a regular pattern consisting of local pockets of laminar flow separation in the vicinity of each particle. These pockets increase in size as the inviscid flow accelerates past the leading edge, and after reaching a certain critical size, they appear to develop fine scale disturbances and quickly transition to turbulence. Transition occurs at a fixed streamwise point in the spanwise directions as seen previously. The Grit 75% case shows a very similar behavior, but because of the randomness in the grit, the transition to turbulence happens earlier and in a less orderly fashion. The Trip Strip 85% case exhibits laminar separation from the trip, forming a recirculation zone behind the trip. This separation evolves into turbulent flow as spanwise instabilities appear. Finally, the Dot Trip case involves a prominent horse shoe vortex that originates just ahead of the cylinder and interacts with the cylinder wake. The wake contains a highly complex flow from its start, and those flow structures appear to quickly break up the horseshoe vortex into turbulence. From these images, it seems that for a given trip height, the Dot Trip produces transition within the shortest distance from the start of the trip.

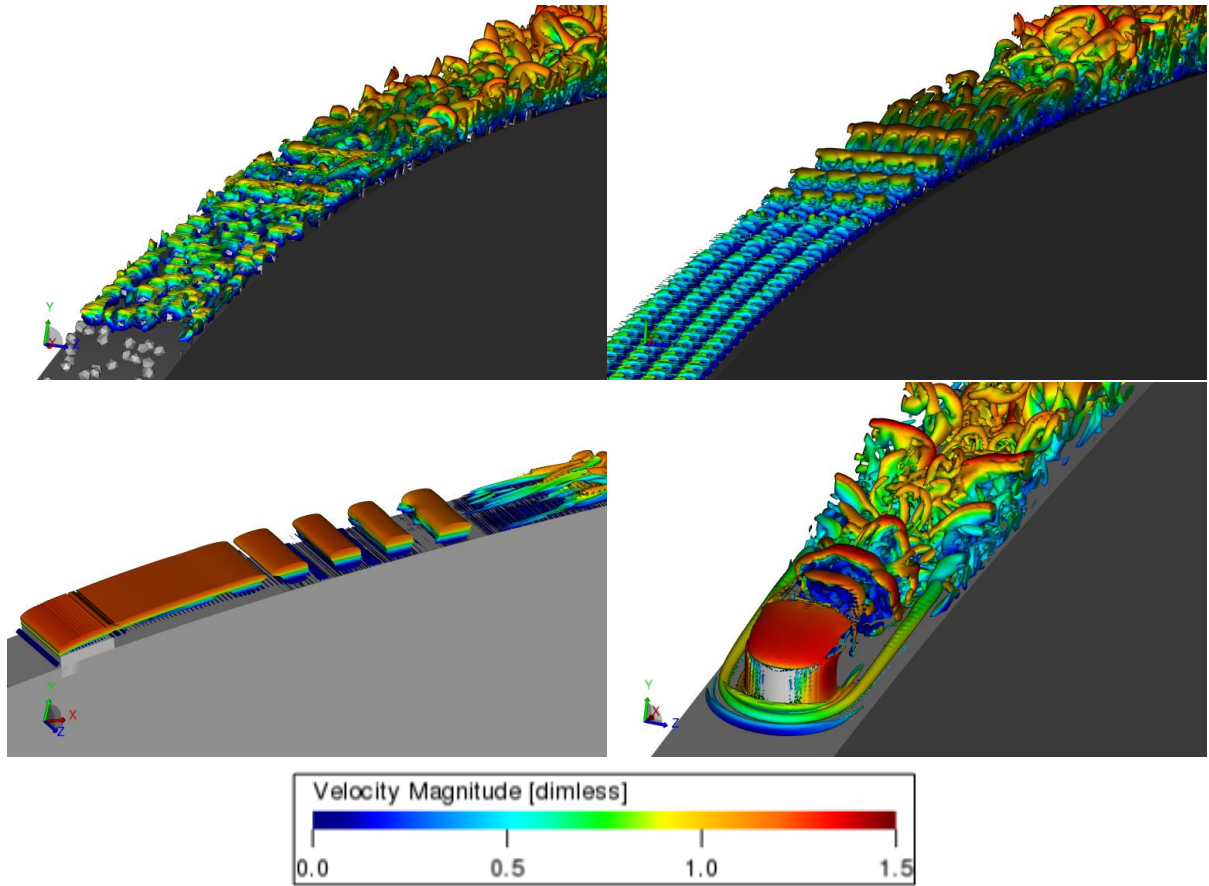


Figure 10: Isosurfaces of λ_2 colored by velocity magnitude for different cases. Top left: Grit 75%, $\lambda_2=-10000$. Top right: Homogeneous Grit, $\lambda_2=-10000$. Bottom left: Trip Strip 85%, $\lambda_2=-1000$. Bottom right: Dot Trip, $\lambda_2=-100000$.

4.3 Spanwise Length Sensitivity for Baseline Grit

Due to the very narrow spans used in the previous subsections, a study of sensitivity of the transition process to the spanwise length of the computational domain is carried out in this subsection. Because increasing the span proportionately increases the simulation cost, both the symmetry plane and the coarser mesh are employed in most of the cases described in this subsection as summarized in Table 3. Based on the results of subsection 4.2, the original Baseline case, with proper refinement over the entire chord is not included in this subsection, and the Coarse TE results with the baseline value of nominal grit height are used herein as reference.

Table 3: Summary of cases for the spanwise length sensitivity study.

Case name	Symmetry	Span (% chord)
Coarse TE	yes	0.625
Coarse TE 2xSpan	yes	1.250
Coarse TE 3xSpan	yes	1.875
Coarse TE 3xSpan NoSym	no	1.875
Coarse TE 7xSpan NoSym	no	4.375

The objective of these runs is to evaluate how large the span needs to be from a hydrodynamic perspective, specifically to minimize the sensitivity of the transition process to the spanwise domain width. TE noise computation in future work will have its own requirements regarding the spanwise length; however, the sensitivity of acoustic predictions to the spanwise domain will not be considered

here, except for performing a couple of runs with no symmetry (NoSym) boundary conditions as stepping stones for the TE noise cases in the future. Note that the latter cases will require both sides of the airfoil, as well as mandating no coarsening near the TE.

Fig. 11 shows $C_{p,RMS}$ over the airfoil chord for the different cases investigated in this subsection. While the transition location is similar among these cases, the levels after the end of the grit change dramatically from the smallest span to the 2xSpan case. This appears to be an indication of the fact that the turbulent structures in the boundary layer are not given enough space to decorrelate across the span for the narrow-span Coarse TE case. All cases with a spanwise domain width equal to or greater than the 2xSpan seem to have very similar $C_{p,RMS}$ levels, with the 2xSpan case having slightly higher levels near the TE, likely due to the shorter span enforcing larger coherence in that area as the turbulence structures continue to grow in size over the chord. This indicates that the results in the previous subsections may have been affected by the spanwise extent of the simulations. Hence future studies should be conducted with larger spans. Another feature that is worth mentioning is the change in the curves at 30% chord, where the grid is coarsened. This happens because the viscosity in the coarse region is effectively doubled to avoid numerical instabilities. This effectively reduces the local Reynolds number by half, which affects all the boundary layer properties.

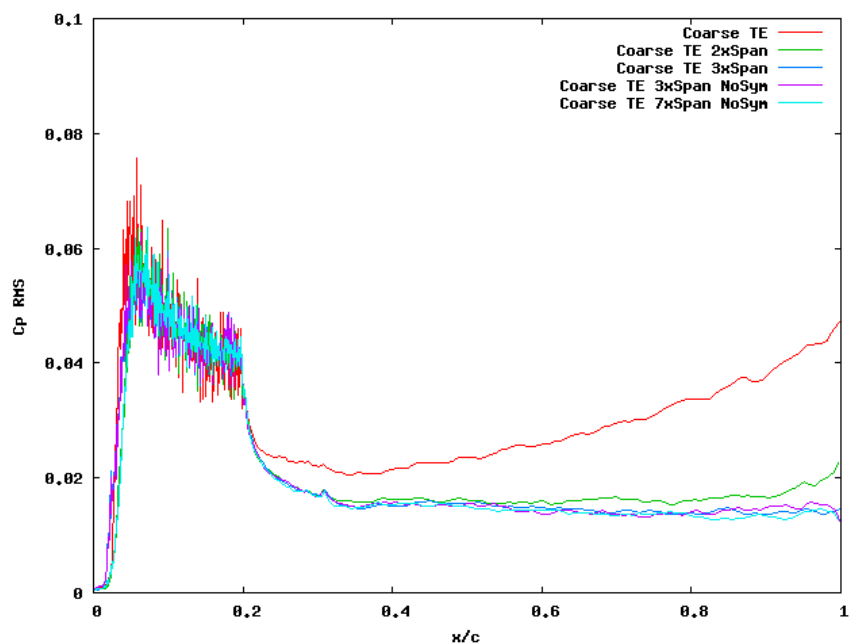


Figure 11: $C_{p,RMS}$ over the airfoil chord for different spans.

Zooming into the LE region, Fig. 12 shows $C_{p,RMS}$ over the first 20% of the chord. Although the levels are very similar after 6% of the chord, the transition location and the slope $C_{p,RMS}$ across the transition zone vary somewhat with the spanwise domain width. This is further investigated in Fig 13, where the surface distribution of $C_{p,RMS}$ is shown. Consistent with subsection 4.1, the Coarse TE 3xSpan and Coarse TE 3xSpan NoSym show almost identical results, indicating that the transition dynamics are not significantly influenced by the symmetry condition for the present flow configuration, and hence, by the upstream propagating acoustic field generated by the scattering of boundary layer eddies near the trailing edge.

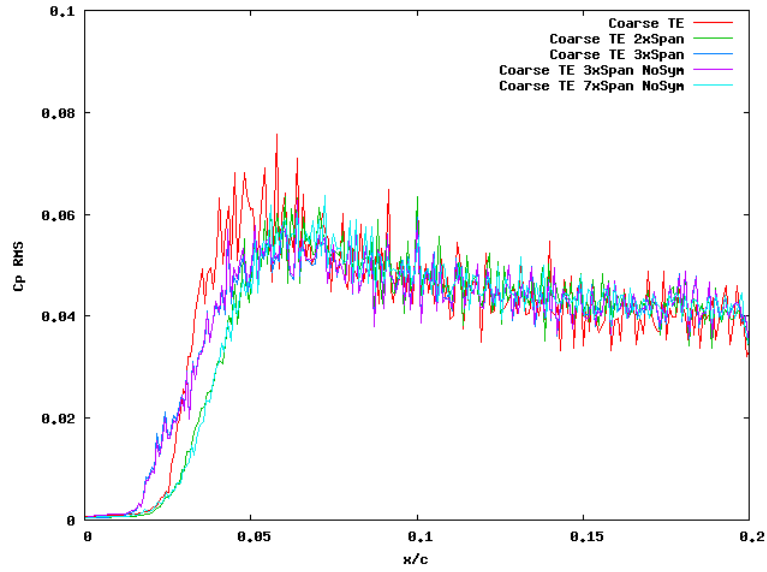


Figure 12: $C_{p,RMS}$ over the airfoil chord for different spans, focused on the leading edge.

Fig. 13 shows a top view of the surface $C_{p,RMS}$ for the four spans outlined in Table 3. For the 3xSpan, results for the Coarse TE 3xSpan NoSym case are not shown, since they look identical to those for the Coarse TE 3xSpan case shown in the figure. The spanwise variation of the transition point, as measured by a sudden rise in $C_{p,RMS}$ is quite noticeable for all four spans, indicating that the similarity in the $C_{p,RMS}$ curves for the 2xSpan and 7xSpan cases in Fig. 12 was rather serendipitous. Interestingly, the surface patterns for the different spans look somewhat similar to each other; for instance, the transition onset front in the 3xSpan case resembles a subset of that in the 7xSpan case, and so on. This would indicate that the transition fronts in these cases are behaving similarly, at least at first glance, but that differences will occur as long as the spanwise domain width is not sufficiently long to capture the larger spanwise scales in the flow, which are greater than the average distance between the particles. The analysis performed thus far does not reveal if the spanwise variations in the transition front would asymptote to some fixed multiple of the mean particle distance or if those variations are also influenced by additional flow parameters such as the boundary layer thickness, Reynolds number, and details of the boundary layer profile. A deeper analysis of the simulation database, including the evolution of spanwise correlation across the transition zone, will be carried out as part of the follow-on effort. Note that all of the $C_{p,RMS}$ vs chord plots that have been shown were made with spanwise averaging of the results.

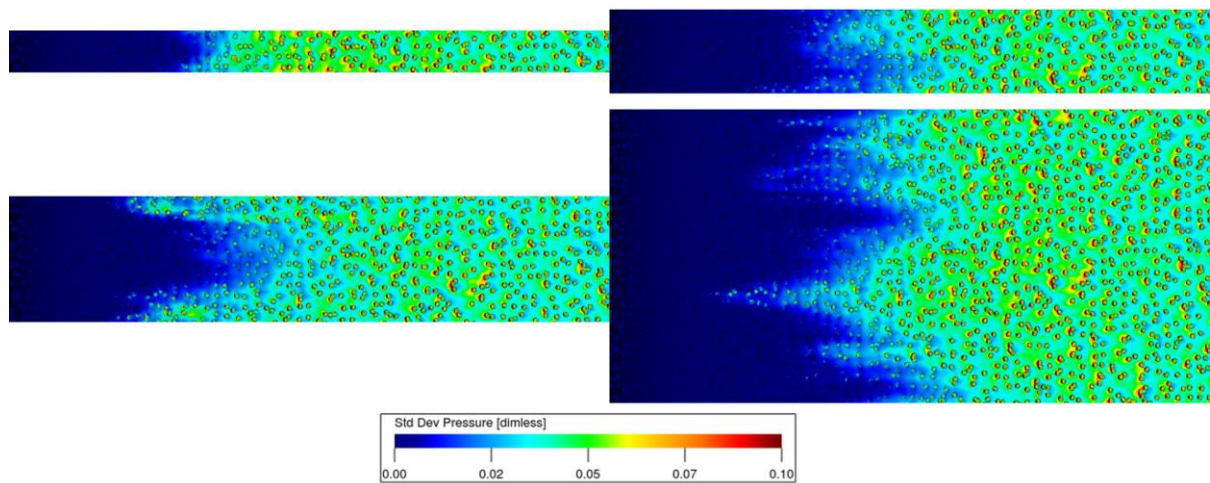


Figure 13: surface distribution of $C_{p,RMS}$ near the transition location. Top left shows the smallest span, top right 2xSpan, bottom left 3xSpan, bottom right 7xSpan.

5 Conclusions and Future Work

The present work has addressed the low Mach number transitional flow over the leading edge of an NACA 0012 airfoil with several types of boundary layer trips, with a primary emphasis on scale resolved, Lattice-Boltzmann simulations in the presence of stochastic sand grain roughness for a chord Reynolds number of 0.657 million. As a prelude to adequately resolved aeroacoustic simulations targeting noise emission from the airfoil trailing edge, the focus of the present effort was on the aerodynamic aspects of the boundary layer flow, and specifically on a parametric study that investigated the sensitivity of the predicted transition location to the height as well as form of the tripping device, mesh resolution, computational domain size, and numerical boundary condition. Refining the mesh in the leading edge region did not have a significant effect on the transition location, which leads to the conclusion that the mesh with a nominal voxel size of $1/40960$ of the chord within the grit region was sufficiently fine to capture the transition due to size 60 grit. The results indicate that using a symmetry plane boundary condition and coarsening the mesh over the aft part of the airfoil also had no significant influence on the transition behavior, which allowed additional simulations for larger spanwise domains. Stochasticity of the realistic grit distributions led to relatively similar spanwise variations in the transition front over a broad range of spanwise domain widths; however, a minimum span of 1.25% of the chord was found necessary to achieve relatively robust predictions of the boundary layer fluctuations at the trailing edge.

The simulations provided interesting insights into the transition process due to different tripping devices. In particular, the Dot Trip, rectangular Trip Strip, and both homogeneous and stochastic grit distributions were observed to exhibit apparently different transition mechanisms. However, in all cases, no sustained external forcing was necessary to initiate the onset of transition. Furthermore, the limited grid refinement permissible within the context of this study as well as the manipulation of the upstream propagating acoustic field from the trailing edge region were found to have no significant influence on the transition process. The grit was found to add the most drag to the airfoil, even when transition occurred after the trip strip cases.

Mesh coarsening beyond 30 percent chord during the larger span simulations introduces extraneous viscosity in the boundary layer flow within that region; however, the comparisons presented in this paper indicate that the grid coarsening approach should produce adequate predictions of the transition behavior on the airfoil. Even though aeroacoustic computations targeting trailing-edge noise require the boundary layer flow to be resolved up to the trailing edge location, the details of the transition process may not be that important, and therefore, a deterministic trip such as the Dot Trip that mimics the transition location produced by the grit is likely to yield acceptable predictions of the acoustics. Future work will build upon the present computations to test that hypothesis.

Boundary layer properties and the drag coefficient of the airfoil agreed reasonably well with the references, with the boundary layer displacement thickness and momentum thickness at the trailing edge being significantly closer to the experimental data compared to previous simulations where the grit was half sunk into the airfoil leading edge.

In closing, the present paper extends the considerable body of work involving airframe noise computations based on Lattice-Boltzmann method by considering DNS of laminar to turbulent transition as a prelude to the DNS of the entire nearfield responsible for TE noise, and potentially, to hybrid simulations that resolve the transition process with DNS, while switching to large eddy simulation in the fully turbulent region downstream.

References

- [1] Choudhari, M., Bahr, C., Khorrami, M.R., Lockard, D.P., Lopes, L., Zawodny, N., Herr, M., Pott-Pollenske, M., Kamruzzaman, M., Van de Ven, T., Manoha, E., Redonnet, S., Yamamoto, K.,

- Ikeda, I., Imamura, T., 2016. Simulations & Measurements of Airframe Noise: A BANC Workshops Perspective. Proceedings of NATO STO-MP-AVT-246 Specialists Meeting on Progress and Challenges in Validation Testing for Computational Fluid Dynamics, Avila, Spain, Sept. 26-28.
- [2] Herr, M., Ewert, R., Rautmann, C., Kamruzzaman, M., Bekiropoulos, D., Iob, A., Arina, R., Batten, P., Chakravarthy, S., Bertagnolio, F., 2015. Broadband Trailing-Edge Noise Predictions Overview of BANC-III Results. AIAA Paper 2015-2847.
- [3] Ffowcs Williams, J.E., Hall, L.H., 1970. Aerodynamic Sound generation by Turbulent Flow in the Vicinity of a Scattering Half-Plane. *Journal of Fluid Mechanics* 40, 657-670.
- [4] Howe, M.S., 1978. A Review of the Theory of Trailing-Edge Noise. *Journal of Sound and Vibration* 61 (3), 437-465.
- [5] Chase, D.M., 1975. Noise Radiated from an Edge in Turbulent Flow. *AIAA Journal* 13, 1041-1047.
- [6] Amiet, R.K., 1976. Noise due to Turbulent Flow Past a Trailing Edge. *Journal of Sound and Vibration* 47 (3), 387-393.
- [7] Khorrami, M., Fares, E. Simulation-Based Airframe Noise Prediction of a Full Scale, Full Aircraft. AIAA Paper 2016-2706.
- [8] Khorrami, M., Duda, B., Hazir, A., Fares, E. Computational Evaluation of Airframe Noise Reduction Concepts at Full Scale. AIAA Paper 2016-2711.
- [9] van der Velden, W.C.P., Oerlemans, S. Numerical analysis of noise reduction mechanisms on improved trailing edge serrations using the Lattice Boltzmann method. AIAA Paper 2017-1379.
- [10] Ribeiro, A.F.P., Casalino, D., Fares, E., Choudhari, M., Direct Numerical Simulation of an Airfoil with Sand Grain Roughness on the Leading Edge. NASA TM-2016-219363.
- [11] Hutcheson, F.V., Brooks, T.F., 2002. Measurement of Trailing Edge Noise Using Directional Array and Coherent Output Power Methods. *International Journal of Aeroacoustics* 1 (4), 329–353.
- [12] Brooks, T.F., Hodgson, T.H., 1981. Trailing Edge Noise Prediction from Measured Surface Pressures. *Journal of Sound and Vibration* 78 (1), 69-117.
- [13] Gershfeld, J., Blake, W.K., Knisely, C.W., 1988. Trailing Edge Flows and Aerodynamic Sound. AIAA Paper 88-3826.
- [14] Migliore, P., Oerlemans, S., 2004. Wind Tunnel Aeroacoustic Tests of Six Airfoils for Use on Small Wind Turbines. *Journal of Solar Energy Engineering* 126 (4), 974-985.
- [15] Brooks, T.F., Pope, D.S., Marcolini, M.A., 1989. Airfoil Self-Noise and Prediction. NASA Reference Publication 1218.
- [16] Slotnick, J., Khodadoust, A., Alonso, J., Darmofal, D., Gropp, W., Lurie, E., Mavriplis, D., 2014. CFD Vision 2030 Study: A Path to Revolutionary Computational Aerosciences. NASA Technical Report, CR-2014-218178.
- [17] Garcia-Sagrado, A., Hynes, T., 2012. Wall Pressure Sources Near an Airfoil Trailing Edge Under Turbulent Boundary Layers. *Journal of Fluids and Structures* 30, 3-34.
- [18] Herrig, A., 2011. Validation and Application of a Hot-Wire Based Method for Trailing-Edge Noise Measurements on Airfoils. Doctoral thesis, Institute of Aerodynamics and Gas Dynamics, Faculty of Aerospace Engineering and Geodesy, University of Stuttgart, Stuttgart, Germany.
- [19] Kerho, M.F., Bragg M.B., 1997. Airfoil Boundary-Layer Development and Transition with Large Leading-Edge Roughness. *AIAA Journal* 35, 75-84.
- [20] Langel, C.M., Chow, R., van Dam, C.P., Maniaci, D.C., Ehrmann, R.S. White, E. B., 2014. A Computational Approach to Simulating the Effects of Realistic Surface Roughness on Boundary Layer Transition. AIAA Paper 2014-0234.
- [21] Sharma, A., Drews, S.D., Kuester, M., Goldstein, D.B., White, E.B., 2014. Evolution of Disturbances due to Distributed Surface Roughness in Laminar Boundary Layers. AIAA Paper 2014-0235.
- [22] Wolf, W.R., Lele, S.K., 2012. Trailing-Edge Noise Predictions Using Compressible Large-Eddy Simulation and Acoustic Analogy. *AIAA Journal* 50, 2423-2434.
- [23] George, J.K., Lele, S.K., 2016. Large Eddy Simulation of Airfoil Self-Noise at High Reynolds Number. AIAA Paper 2016-2919.
- [24] Winkler, J., Moreau, S., Carolus, T., 2009. Large-Eddy Simulation and Trailing-Edge Noise

- Prediction of an Airfoil with Boundary-Layer Tripping. AIAA Paper 2009-3197.
- [25]Chen, H., Teixeira, C., Molvig, K., 1997. Digital Physics Approach to Computational Fluid Dynamics: some basic theoretical features. *International Journal of Modern Physics C* 8 (4), 675-684.
- [26]Chen, S., Doolen, G.D., 1998. Lattice Boltzmann Method for Fluid Flows. *Annual Review of Fluid Mechanics* 30, 329-364.
- [27]Courant, R., Friedrichs, K., Lewy, H., 1928. Über die partiellen Differenzgleichungen der mathematischen Physik. *Mathematische Annalen* 100 (1), 32-74.
- [28]Bhatnagar, P.L., Gross, E.P., Krook, M., 1954. A Model for Collision Processes in Gases. I. Small Amplitude Processes in Charged and Neutral One-Component Systems. *Physical Review* 94 (3), 511-525.
- [29]Fan, H., Zhang, R., Chen, H., 2006. Extended Volumetric Scheme for Lattice Boltzmann Models. *Physical Review E* 73, 066708.
- [30]Chen, H., Teixeira, C., 2000. H-Theorem and Origins of Instability in Thermal Lattice Boltzmann Models. *Computer Physics Communications* 129, 21-31.
- [31]Chapman, S., Cowling, T., 1990. *The Mathematical Theory of Non-Uniform Gases*, Cambridge University Press, London.
- [32]Chen, H., Chen, S., Matthaeus, W.H., 1992. Recovery of the Navier-Stokes Equations Using a Lattice-Gas Boltzmann Method. *Physical Review A* 45 (8), 5339-5342.
- [33]Qian, Y.H., D’Humières, D., Lallemand, P., 1992. Lattice BGK Models for Navier-Stokes Equation. *Europhysics Letters* 17 (6), 479-484.
- [34]Shan, X., Yuan, X.-F., Chen, H., 2006. Kinetic Theory Representation of Hydrodynamics: A Way Beyond the Navier-Stokes Equation. *Journal of Fluid Mechanics* 550, 413-441.
- [35]Chen, H., Kandasamy, S., Orszag, S., Shock, R., Succi, S., Yakhot, V., 2003. Extended Boltzmann Kinetic Equation for Turbulent Flows. *Science* 301 (5633), 633-636.
- [36]Chen, H., Teixeira, C., Molvig, K., 1998. Realization of Fluid Boundary Conditions via Discrete Boltzmann Dynamics. *International Journal of Modern Physics C* 9 (8), 1281-1292.
- [37]Li, Y., Shock, R., Zhang, R., Chen, H., 2004. Numerical Study of Flow Past an Impulsively Started Cylinder by Lattice Boltzmann Method. *Journal of Fluid Mechanics* 519, 273-300.
- [38]Sanjosé, M., Méon, C., Masson, V., Moreau, S., 2014. Direct Numerical Simulation of Acoustic Reduction Using Serrated Trailing-Edge on an Isolated Airfoil. AIAA Paper 2014-2324.
- [39]Ribeiro, A.F.P., Casalino, D., Fares, E., 2016. Lattice-Boltzmann Simulations of an Oscillating NACA0012 Airfoil in Dynamic Stall. In Braza, M., Bottaro, A., Thompson, M. ed., *Advances in Fluid-Structure Interaction*, Springer, 179-192.
- [40]Koenig, B., Fares, E., Ishikawa, K., Murayama, M., Ito, Y., Yokokawa, Y., Yamamoto, K., 2016. Lattice-Boltzmann Simulations of the JAXA JSM High-Lift Model. AIAA Paper 2016-3721.
- [41]Casalino, D., Noelting, S., Fares, E., Van de Ven, T., Pérot, F., Brès, G., 2012. Towards Numerical Aircraft Noise Certification: Analysis of a Full-Scale Landing Gear in Fly-Over Configuration. AIAA Paper 2012-2235.
- [42]Drela, M., 1989. XFOIL: An Analysis and Design System for Low Reynolds Number Airfoils. *Conference on Low Reynolds Number Airfoil Aerodynamics*. University of Notre Dame.
- [43]Jeong, J., Hussain, F., 1995. On the Identification of a Vortex. *Journal of Fluid Mechanics* 285, 69-94.